

Doppler and modulation tomography of XTE J1118+480 in quiescence

D.E. Calvelo,^{1,2} S.D. Vrtilik,¹ D. Steeghs,^{1,3} M.A.P. Torres,¹ J. Neilsen,^{1,4}
A.V. Filippenko,⁵ and J.I. González Hernández,^{6,7}

¹ *Harvard-Smithsonian Center for Astrophysics, 60 Garden Street, Cambridge, MA 02138, USA*

² *School of Physics and Astronomy, University of Southampton, Highfield, Southampton, SO17 1BJ, UK*

³ *Department of Physics, University of Warwick, Coventry, CV4 7AL, UK*

⁴ *Harvard University, Department of Astronomy, 60 Garden Street, MS-10, Cambridge, MA 02138, USA*

⁵ *Department of Astronomy, University of California, Berkeley, CA 94720-3411, USA*

⁶ *Observatoire de Paris-Meudon, GEPI, 5 place Jules Janssen, 92195 Meudon Cedex, France*

⁷ *CIFIST Marie Curie Excellence Team*

30 October 2018

ABSTRACT

We present Doppler and modulation tomography of the X-ray nova XTE J1118+480 with data obtained during quiescence using the 10-m Keck II telescope. The hot spot where the gas stream hits the accretion disc is seen in $H\alpha$, $H\beta$, $He\ I\ \lambda 5876$, and $Ca\ II\ \lambda 8662$, thus verifying the presence of continued mass transfer within the system. The disc is clearly seen in $H\alpha$ and $Ca\ II\ \lambda 8662$. We image the mass-donor star in narrow absorption lines of $Na\ I\ \lambda\lambda 5890, 5896, 8183, 8195$ and $Ca\ II\ \lambda 8662$, implying an origin from the secondary itself rather than the interstellar medium. We also detect deviations in the centroid of the double peak of $H\alpha$ akin to those found by Zurita et al. 2002 suggesting disc eccentricity.

Key words: accretion, accretion discs – binaries: close – stars: individual, XTE J1118+480

1 INTRODUCTION

XTE J1118+480 is a member of a subclass of low-mass X-ray binaries (LMXBs) known as X-ray novae (XRNe) or soft X-ray transients. These are systems in which the low-mass companion fills its Roche lobe, resulting in accretion onto the heavier primary (a neutron star or black hole). The XRNe in particular undergo significant luminosity variations over time; they occur as “outburst” events involving rapid increases in X-ray light by many orders of magnitude over timescales of days, coupled with a noticeable increase in optical light. Systems can remain in outburst for months before declining into an epoch of quiescence where they may remain for decades before undergoing another similar event (e.g., Chen, Shrader, & Livio 1997).

The cause and processes behind such events are yet to be made clear. One of the more favored explanations involves the application of disc instability models (Meyer & Meyer-Hofmeister 1981). Such theories were originally conceived for discs in cataclysmic variable systems but can also be applied to discs that form around the primaries of LMXBs. The quiescent state can be regarded as a period where the disc gains mass and evolves until it reaches a critical point and destabilizes, resulting in large quantities of mass being

dumped onto the primary in a short period of time, in turn causing the outburst we see.

XTE J1118+480 was discovered during an outburst (Remillard et al. 2000) on 2000 March 29 (UT dates are used throughout this paper) by the Rossi X-ray Timing Explorer (RXTE; Jahoda et al. 1996) All-Sky Monitor (ASM; Levine et al. 1996). Its optical counterpart (brightening to $V \approx 12.9$ mag during outburst) was discovered in the same year by Uemura, Kato, & Yamaoka (2000a), corresponding to an 18.8 mag star in USNO catalogues. A 4.1 hr period was detected by several independent investigations (Patterson et al. 2000; Uemura et al. 2000b), and distortions within light curves were attributed to superhumps (Uemura et al. 2000c; Zurita et al. 2002, henceforth Zu02; Zurita et al. 2006; Torres et al. 2004, henceforth To04). Such phenomena theoretically occur when the accretion disc expands to encompass tidal resonance radii, triggering precessional effects on the disc due to the gravitational pull of the secondary star (Whitehurst & King 1991). The deformed disc then causes intensity variations as its projected area varies with phase.

XTE J1118+480 was also observed in a “mini-outburst” state in 2005 by Zurita et al. (2006), who noted that the sys-

Table 1. XTE J1118+480 System Parameters

Orbital period	0.16995 ± 0.00012 d ⁽¹⁾
HJD phase 0	$2453049.93346 \pm 0.00007$ d ⁽¹⁾
Mass Ratio q (M_2/M_1)	0.024 ± 0.009 ⁽³⁾
	0.0435 ± 0.0100 ⁽²⁾
Inclination	$68^\circ \pm 2^\circ$ ⁽²⁾
$v \sin i$	96_{-11}^{+3} km s ⁻¹ ⁽³⁾
Primary Object Mass	$8.53 \pm 0.60 M_\odot$ ⁽²⁾
Mass Function	$6.27 \pm 0.04 M_\odot$ ⁽¹⁾
K_2	708.8 ± 1.4 km s ⁻¹ ⁽¹⁾
Systemic velocity γ	2.7 ± 1.1 km s ⁻¹ ⁽¹⁾
Distance	1.72 ± 0.10 kpc ⁽²⁾
Secondary spectral type	K5 V ⁽¹⁾

Note: ⁽¹⁾González Hernández et al. (2008). ⁽²⁾Gelino et al. (2006). ⁽³⁾See Section 2. The Gelino et al. parameters were calculated in conjunction with a different mass ratio and thus we include both values for reference.

tem exhibited superhump activity during the mini-outburst before settling back into quiescence.

Subsequent observations since the discovery of XTE J1118+480 have yielded well-constrained system parameters. Radial-velocity measurements of the secondary star carried out during the post-outburst period gave a mass function of $\sim 6 M_\odot$ (McClintock et al. 2001a; Wagner et al. 2001; González Hernández et al. 2006, hereafter GH06), providing evidence that the compact object is a black hole. Since superhump modulations can alter the apparent ephemeris, observations of XTE J1118+480 in quiescence (which presumably lacks superhump activity) have allowed for refinement of many system parameter measurements including the period (Gelino et al. 2006; González Hernández et al. 2008, hereafter GH08). Gelino et al. (2006) improved the determination of the inclination angle (to $68^\circ \pm 2^\circ$) which constrained the mass of the primary to $8.53 \pm 0.60 M_\odot$, confirming its identification as a black hole. System parameter values, including those used in calculations herein, are listed in Table 1.

Doppler tomography (Marsh & Horne 1988) has been applied to XTE J1118+480 several times since its discovery. Dubus et al. (2001) produced He II and H α tomograms from observations taken on 2000 April 20, while the system was in outburst. A bright region in the maps was attributed to a hot spot where the accretion stream interacts with the disc. Torres et al. (2002, henceforth To02) produced tomograms for the nights of 2000 March 31, April 12 and 29, and May 25 (during the same outburst), revealing a disc as well as a “bow-shaped” emission region whose position suggested ties with the accretion stream or a stream-disc interaction.

The most recent tomograms produced prior to those in this paper are found in To04 and Elebert et al. (2006). The To04 observations were taken on the nights of 2000 Dec. 29, 2001 Jan. 26, and 2003 Jan. 2 and 3 in order to cover decline into quiescence and quiescence itself. A possible hot spot was observed in both the 2000 and 2001 images, as well as evidence for a precessing eccentric disc. Also apparent was a second bright region perhaps due to accretion-stream overflow. Most interestingly, although a disc is apparent, no hot-spot region was detected in the To04 2003 tomogram. The asymmetric component of the 2003 map revealed H α emission centered on the companion’s Roche lobe rather than

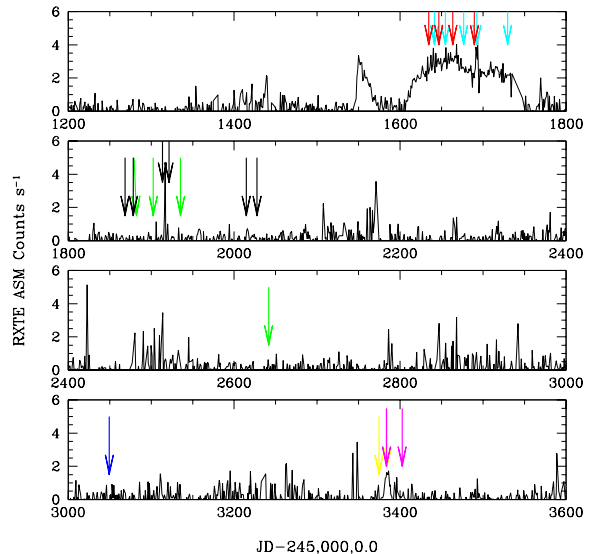


Figure 1. RXTE ASM light-curve data for XTE J1118+480. Data were retrieved using the ASM data website at <http://xte.mit.edu/ASM.Lc.html>. Arrows indicate the times of optical observations. Cyan = Dubus et al. (2001); black = Zurita et al. (2002; no tomography); red = Torres et al. (2002); green = Torres et al. (2004); blue = current work; yellow = Zurita et al. (2006; no tomography); magenta = Elebert et al. (2006).

at a position which could be attributed to a hot spot. The implication is that a change in accretion rate had occurred since the earlier observations. Surprisingly, Doppler tomograms by Elebert et al. (2006) of observations taken during the 2005 mini-outburst also do not show a significant hot spot in H α . The timings of relevant XTE J1118+480 optical observations are shown in Figure 1 against the system’s X-ray intensity.

In this paper we produce Doppler and modulation tomography maps of XTE J1118+480 from Keck II observations taken on 2004 Feb. 14, when the system was well into quiescence. One of the shortcomings of Doppler tomography is that it assumes emission is constant over the orbit. Modulation tomography (Steeghs 2003) addresses this problem and hence can reveal the structure of accretion flow in greater detail. Our observations represent greater than a factor of 4 improvement in spectral resolution over previous observations used for tomography of XTE J1118+480. The higher spectral resolution, in addition to improved orbital phase resolution, enabled us to produce detailed modulation tomography maps of H α , the strongest line. We search for evolutionary trends by comparing our tomograms with those taken at different outburst phases.

2 OBSERVATIONS

The observations used in this paper were initially described by GH06. They consist of 74 medium-resolution ($\lambda/\Delta\lambda \approx 6,000$) spectra of XTE J1118+480 taken on 2004 Feb. 14, using the Echellette Spectrograph and Imager (Sheinis et al. 2002) on the 10-m Keck II telescope. Table 2 lists the observations and the associated orbital phase calculated using

Table 2. Journal of Observations on 2004 February 14.

Record	UTC	Phase	Record	UTC	Phase
1	7.86802	-0.5956	38	11.80850	0.3705
2	7.97901	-0.5684	39	11.91085	0.3956
3	8.08408	-0.5426	40	12.01332	0.4207
4	8.19076	-0.5165	41	12.11583	0.4458
5	8.30549	-0.4883	42	12.21775	0.4708
6	8.41041	-0.4626	43	12.35703	0.5050
7	8.51713	-0.4365	44	12.45861	0.5299
8	8.65651	-0.4023	45	12.56290	0.5555
9	8.76902	-0.3747	46	12.66709	0.5810
10	8.87278	-0.3493	47	12.76956	0.6061
11	8.97658	-0.3238	48	12.87331	0.6316
12	9.08021	-0.2984	49	12.97488	0.6565
13	9.17981	-0.2740	50	13.07572	0.6812
14	9.27935	-0.2496	51	13.17689	0.7060
15	9.38655	-0.2233	52	13.30560	0.7375
16	9.51406	-0.1920	53	13.41519	0.7644
17	9.61566	-0.1671	54	13.51554	0.7890
18	9.71547	-0.1426	55	13.61731	0.8140
19	9.81456	-0.1184	56	13.71921	0.8389
20	9.92418	-0.0915	57	13.82052	0.8638
21	10.02500	-0.0668	58	13.92143	0.8885
22	10.12409	-0.0425	59	14.02387	0.9136
23	10.22280	-0.0183	60	14.13096	0.9399
24	10.36291	0.0161	61	14.27274	0.9746
25	10.46241	0.0405	62	14.39129	1.0037
26	10.56251	0.0650	63	14.49344	1.0288
27	10.66197	0.0894	64	14.59468	1.0536
28	10.76201	0.1139	65	14.71055	1.0820
29	10.86116	0.1382	66	14.80933	1.1062
30	10.96110	0.1627	67	14.91224	1.1314
31	11.06149	0.1874	68	15.18856	1.1992
32	11.16561	0.2129	69	15.28683	1.2233
33	11.26717	0.2378	70	15.38589	1.2476
34	11.39890	0.2701	71	15.48483	1.2718
35	11.50254	0.2955	72	15.58512	1.2964
36	11.60421	0.3204	73	15.68769	1.3216
37	11.70602	0.3454	74	15.78674	1.3458

Note: The orbital phase values in columns 3 and 6 are computed using the orbital solution from GH08.

the ephemeris determined by GH08 and listed in Table 1. All spectra were reduced in a standard manner as described by GH06.

3 SPECTRAL ANALYSIS

3.1 Spectra

The smearing of lines due to the motion of the star during a given exposure was incorrectly determined by González Hernández et al. (GH06). However, this has a small impact in the derived rotational velocity. We have determined the smearing to be in the range 2–90 km s⁻¹. Our new value for the rotational velocity is $v \sin i = 96_{-11}^{+3}$ km s⁻¹ (originally = 100_{-11}^{+3} km s⁻¹ in GH08), where the uncertainties have been derived by assuming extreme cases for the linearized limb-darkening $\epsilon = 0 - 1$. This rotational velocity combined with the GH08 value of the secondary-star radial-velocity semi-amplitude, K_2 , implies a binary mass ratio $q = 0.024 \pm 0.009$ (originally = 0.027 ± 0.009).

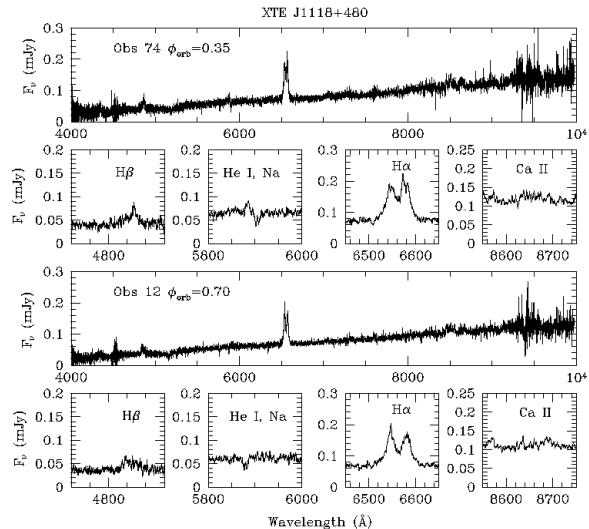


Figure 2. Sample spectra from two orbital phases with close-ups of some of the line features. Upper panels: orbital phase 0.35. Lower panels: orbital phase 0.70. Data have been smoothed with a boxcar of width 7 pixels.

The reduced spectra were examined for spectral features suitable for use in tomography studies. The strongest lines (H α , H β , and Ca II) show significant structure in their profiles, and are thus good candidates. The sensitivity of our data also allowed us to study the much weaker lines of He I $\lambda 5876$ and Na I $\lambda\lambda 5890, 5896, 8183, 8194$.

The spectra were analyzed using the MOLLY software developed by Tom Marsh. We concentrate on six spectral regions that cover the brightest lines (H α , H β , He I/Na I, Na I absorption near $\lambda 8200$, and several lines of Ca II). Sample spectra from two orbital phases are shown in Figure 2: the double-peak structure associated with rotating disc emission is clearly evident in H α . As the strongest visible emission line (average equivalent width of about 0.5 \AA), H α is the best defined. The location of H β near the blue end of the spectrum (where device sensitivity begins to drop) and its relatively low intensity (factor of ~ 4 weaker than H α ; average equivalent width around 0.12 \AA) means that there is substantially more noise and the double-peak structure is harder to detect. The double-peak structure is not resolved in He I, and is blended in Ca II because of overlap between closely spaced emission and absorption features.

3.2 H α Variability

The emission lines of XTE J1118+480 are known to exhibit strong asymmetric structure as well as variations of emission-line centroid position over time scales far longer than the orbital period (To02; Zu02). Unlike absorption lines which remain centered at the same wavelength (with only the small deviation caused by $\gamma = 2.7$ km s⁻¹), the repeating variance of these emission-line shifts means they cannot be attributed to the systemic velocity. Zu02 fitted a three-component Gaussian (consisting of a broad base and two narrow peaks) to their H α profiles, averaged over each night. They found that the positions of the blue and red peaks are not equidistant from the expected rest wavelength and

Table 3. H α centroid offsets.

Date	V_b	V_r	$V_r - V_b$	V_{off}
2000 Mar 31	-643 ± 24	598 ± 20	1241 ± 31	-22.5 ± 15.5
2000 Apr 12	-601 ± 29	521 ± 17	1122 ± 34	-40.0 ± 17
2000 Apr 29	-576 ± 14	620 ± 25	1196 ± 29	22 ± 14.5
2000 Nov 20	-750 ± 50	950 ± 50	1700 ± 70	100 ± 35
2000 Nov 30	-1050 ± 50	600 ± 50	1650 ± 70	-225 ± 35
2000 Dec 4	-1163 ± 34	664 ± 14	1827 ± 37	-250 ± 18.5
2000 Dec 24	-644 ± 16	1021 ± 23	1665 ± 28	188 ± 14
2000 Dec 29	-651 ± 8	1120 ± 17	1771 ± 19	234 ± 9.5
2001 Jan 4	-600 ± 50	1100 ± 50	1700 ± 70	250 ± 35
2001 Jan 12	-900 ± 50	650 ± 50	1550 ± 70	-125 ± 35
2001 Jan 26	-1134 ± 12	627 ± 7	1761 ± 14	-254 ± 7
2001 Apr 15	-700 ± 50	1000 ± 100	1700 ± 110	150 ± 55
2001 Apr 16	-500 ± 50	950 ± 50	1450 ± 70	225 ± 35
2001 Apr 27	-800 ± 50	800 ± 50	1600 ± 70	0 ± 35
2001 Apr 28	-850 ± 50	750 ± 50	1600 ± 70	-50 ± 35
2003 Jan 2	-952 ± 6	811 ± 8	1763 ± 10	-71 ± 5
2003 Jan 3	-1009 ± 6	823 ± 8	1832 ± 10	-93 ± 5
2004 Feb 14	-786 ± 4	894 ± 4	1680 ± 6	55 ± 3
2005 Jan 12	-662 ± 11	681 ± 11	1343 ± 16	9 ± 8
2005 Feb 1	-843 ± 17	809 ± 11	1652 ± 20	-17 ± 10

Note: Offsets are determined using spectra averaged over each night (for nights when there is coverage over a full binary orbit). All velocities are in km s^{-1} . $V_{\text{off}} = (V_r + V_b)/2$. Numbers before 2004 are from To02, Zu02, and To04. The values with particularly large uncertainties are those read off of Figure 7 in Zu02.

measured offsets up to 300 km s^{-1} . Fitting a sinusoid to the H α offsets they measured on six nights, they found the variations to be consistent with either the precession period of ~ 52 days that they inferred from measurement of a superhump period or half the precession period (~ 26 days; see their Fig. 5). H α offsets measured by To04 (see their Fig. 5) two years after the Zu02 observations were consistent with the precession period but ruled out the 26 day period. Simulations by Faulkes et al. (2004) give convincing evidence that such long time-scale modulations of broad emission lines can be directly linked to the precession of an eccentric, asymmetric disc. In essence, the precession alters the angle at which we observe the elliptical orbit of matter in the disc, thereby causing the velocities we observe at the blue and red “edges” of the disc to oscillate with the precession period.

We measured the H α centroid offset of our observations, which were obtained about one year after the To04 observations, in two ways. First we averaged all 74 observations and fitted three Gaussians to the average profile as was done by Zu02 and To04 (after accounting for γ). We also measured the central velocity and peak-to-peak separation for each spectrum individually and then fit to the system’s radial-velocity to determine the offset. Both methods agree to well within one sigma. We find an overall redward deviation from the rest wavelength (6562.87 \AA) of 1.2 \AA that corresponds to an offset of $54.6 \pm 4 \text{ km s}^{-1}$.

We searched the literature for further examples of H α centroid offset measurements. To the 8 points originally plotted by Zu02 and the 4 points added by To04, we add 3 points from To02 and an additional 2 points from To04 (not included in their Fig. 5 but appearing in their Table 3). We

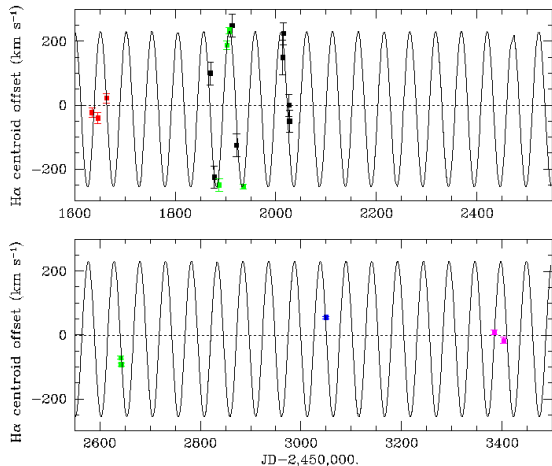


Figure 3. H α centroid offsets. The black points represent Zu02, red points To02, and green points To04 measurements; current observations are in blue; and magenta points are calculated from data presented by Elebert et al. (2006). A sinusoid having a period of 51.42 days (with amplitude and T_0 from To04) is overplotted.

also add 2 points from reanalyzing data obtained by Elebert et al. (2006) approximately one year after our Keck observations, for a total of 20 measurements of the H α offset. We list these values in Table 3 and plot them in Figure 3. We use our offset value to refine the precession period to $P_{\text{prec}} = 51.42 \pm 0.05$ days.

We do not have sufficient points to perform a periodogram, but find by trial and error that a period of 51.42 days (maintaining the amplitude and T_0 as determined by To04) gives the least χ^2 deviation for all of the measured values:

$$V_{\text{offset}} = 243.53 \sin[(2\pi/P_{\text{prec}})(t - T_0)] - 12.56, \quad (1)$$

where $T_0 = \text{JD } 2,451,870.01$. Comparing this fit to the observation times displayed in Figure 1, we would be tempted to believe that precession remains stable over long periods of time regardless of the system’s state. Since the disc of J1118+480 is relatively small (with larger peak-to-peak velocities) and has been shown to vary in size, such unvarying precession behaviour (in both semi-amplitude and period) would be surprising; all tidal models are very sensitive to the size of the accretion disc. However, the sparse and irregular data spacing makes the fit of a single precession period, semi-amplitude, and phase offset highly uncertain, especially if we consider the possibility that these parameters vary with time. Any existing variation can only be investigated via a greater sampling of data points from a range of different epochs, specifically different precession phases.

The peak-to-peak velocity separation ($V_r - V_b$) is noticeably smaller during outburst (2000 Mar–Apr and 2005 Jan 12) than during quiescence. These peak-to-peak velocity changes are well known in cataclysmic variable stars: the disc is large (thus exhibiting a small peak-to-peak separation) during outburst and then shrinks (i.e., the peak separation widens) in quiescence. We note that the Ca II $\lambda 8662$ emission line also shows a strong disc signature in the form of double-peak line profiles. However, we were unable to ob-

tain a satisfactory fit to the Ca II emission lines with the three-Gaussian model because of blending with other lines. We did not attempt any fits for He I and H β since He I also suffers interference from nearby features and the disc signature in H β is weak.

If the disc is large enough to encompass tidal resonance radii, then we would have a plausible explanation for any effects implying the existence of an eccentric precessing disc. The peak-to-peak width of H α in the 2004 Feb 14 data is 36.93 ± 0.1 Å, corresponding to a velocity difference of 1680 ± 5.7 km s⁻¹. Following Dubus et al. (2001), we can make an estimate of the outer disc radius,

$$R_d/a = (1 + q)(2K_2/\Delta V)^2, \quad (2)$$

where ΔV is the peak-to-peak separation. With the ΔV of H α and using K_2 and q from Table 1, we get $R_d/a \approx 0.73 \pm 0.01$, close to the predicted tidal truncation radius ($\sim 0.9R_{\text{Roche}}$, where R_{Roche} is the primary's Roche-lobe radius) of $R_T/a \approx 0.6$ for $q = 0.024$ (King 1995). It should be noted that the s -wave contribution to the H α emission will have at least some effect on the measured ΔV (as in H β) which would result in a small overestimation of R_d . The calculated outer radius exceeds both the 3:1 tidal resonance radius $R_{3:1}/a \approx 0.48$, and the 2:1 resonance radius $R_{2:1}/a \approx 0.62$ (Whitehurst & King 1991). Thus, even in quiescence, the disc appears to be large enough to access its tidal resonance radii.

It should be stressed that Equation 2 is valid only when the orbital motion of matter in the disc is Keplerian. Near outburst the disc is expected to have grown to a point where it is susceptible to destabilisation, and we have little understanding of the behaviour of the disc matter. Hence, points in Table 3 that are measured during outburst when used with Equation 2 give radii that are larger than the binary separation. However, we are effectively left with two scenarios; either the disc is small enough for us to believe the assumptions of Keplerian motion and thus the use of Equation 2, or the disc is sufficiently large (e.g., reaching the truncation radius) to render Equation 2 useless. We only intend to show that the disc can access resonance radii in order to explain any eccentricity effects in the system, which for our calculations is true at both limits.

4 TOMOGRAPHY

Doppler imaging allows us to create a two-dimensional velocity-space image of emission within a binary system using spectra and an accurate ephemeris (Marsh & Horne 1988). The spectra are considered projections of the disc in a single phase direction and are combined using a mathematical inversion technique to produce a model that fits the data. We use the maximum entropy method (MEM) to improve constraints on image selection. MEM includes image entropy as a variable to ensure that the resulting images are as smooth (and thus as physically realistic) as possible. We begin with an arbitrary starting image (e.g., uniform or a Gaussian peak) which is modified to fit the data using a reduced χ^2 test; this process is iterated until a satisfactory fit is achieved, while at the same time maximising the entropy of the reconstructed image.

The trailed spectrograms in Figure 4 (covering the

wavelength ranges of interest) reveal far more detail than the individual spectra. The double-peak profiles of H β become distinct and several weak absorption features can be seen. More importantly, the weaker features of He I and Na I are clearly resolved. The phase delay seen between He I and Na I in the upper-middle panel of Figure 4, as well as between H β and the absorption features in the upper-left panel of Figure 4, points to their originating from different regions of the binary. The faint, barely detectable, vertical lines at 5890 Å and 5896 Å, which show no Doppler effect from the binary motion, appear to be in emission and thus cannot be due to interstellar absorption but likely arise from residual night-sky emission (Na). The Ca II triplet in emission clearly shows the double-peak structure expected from disc emission, and the Ca II absorption features show the same phase delay as the Na I absorption lines.

The continua immediately adjacent to the lines of interest were fitted (while masking the line) and then subtracted to give an average of zero (as required by the Doppler tomography package, DOPPLER, written by Tom Marsh). Spectra were then rebinned to a uniform velocity scale with corresponding laboratory rest wavelengths as origins (the system velocity is applied at a later stage). Spectra were then ready for use in DOPPLER. It should be stressed that only the systemic velocity was accounted for while making these Doppler maps; the 54.6 km s⁻¹ offset was not included.

4.1 Doppler maps

Figures 5–8 display the results of Doppler tomography on four of our regions of interest. Figure 5 shows the images created from H α emission. We can clearly make out a circular disc, but most obvious is the intense bright spot in the $(-V_x, +V_y)$ quadrant. Since the region does not coincide with the secondary star Roche lobe, its origin must be due to a stream/disc interaction hot spot. The hot spot does not lie over either of the trajectories, but this is not unexpected. Collision of the stream with the disc can produce a shock front as the stream's ballistic motion is altered by mixing with the bulk motion of disc material. Consequently, the velocity of matter that passes the shock front should be a blend of the two, causing the emission region to lie between the trajectories, just inside the outer edge of the disc, as observed here. The same behaviour has also been seen in other systems (e.g., A0620–00; Marsh, Robinson, & Wood 1994; Neilsen, Steeghs, & Vrtilik 2008). The spot also appears to be extended along the trajectories, which could be due to the matter stream penetrating deeply into the disc before finally being deviated.

The predicted data reproduce much of the original structure but appear to eliminate the one-sided variation in both the double peak and s -wave signals. This is an example of Doppler tomography not being able to incorporate variable line flux into its modelling (this problem can be removed using modulation tomography; see Section 4.2). The variation we do see in the predicted data arises from the asymmetric shape of the hot spot, and rotational symmetry duplicates the variation in both sides of the profile.

The disc itself appears to be circular, with no distinct features other than the hot spot. Any asymmetric behaviour is better observed in the right-hand column. Since it is inherently asymmetric, we expected the hot spot to reappear

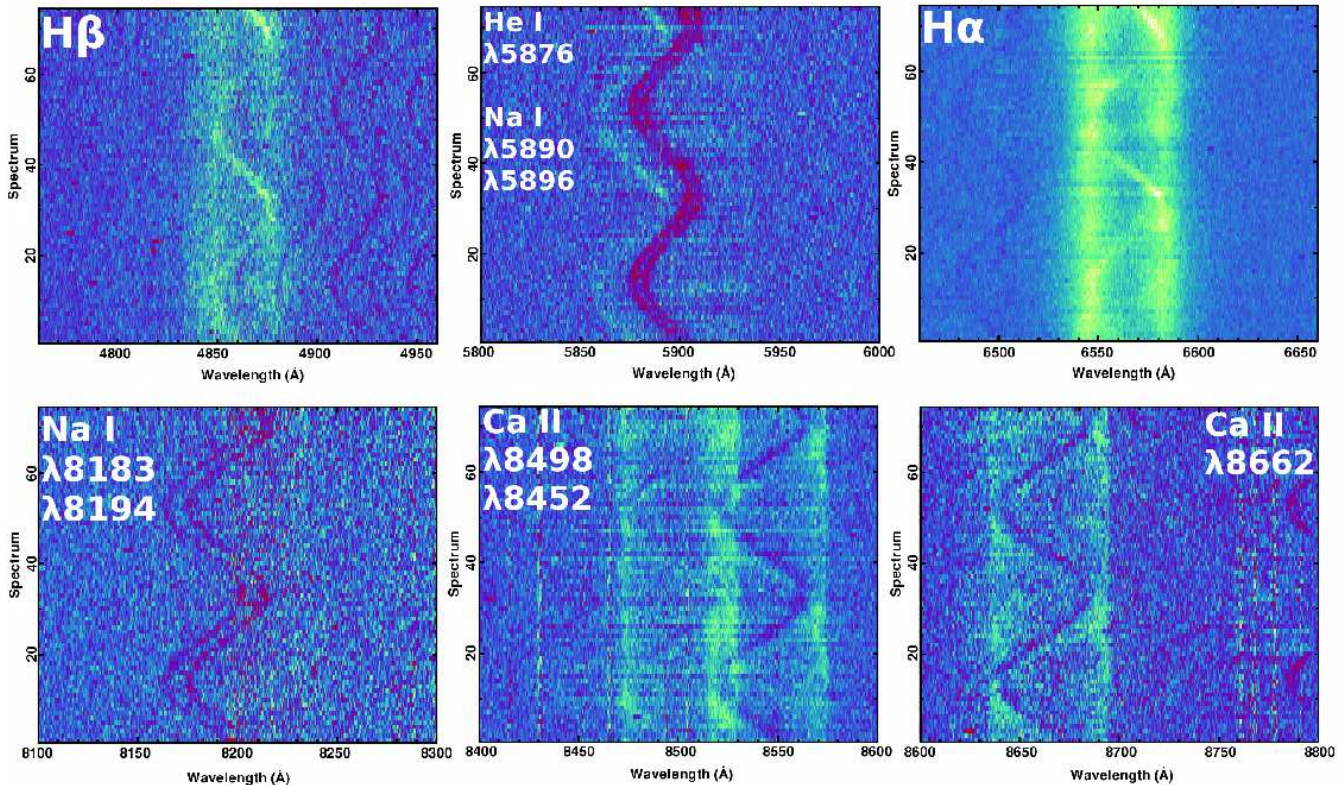


Figure 4. Trailed spectrograms. Upper left: The strong emission (green) feature is H β and several weaker absorption (red) lines are visible to the right. Upper middle: He I in emission and Na I D lines in absorption; also an unidentified faint absorption feature to the left of He I. Upper right: H α in emission and a faint absorption feature to its left. Lower left: Na I λ 8200 doublet in absorption. Lower middle: Ca II triplet seen in both emission and absorption. Lower right: Another Ca II line in both emission and absorption.

in the asymmetric-component data and maps, and it does so relatively unchanged. However, though the disc appeared nearly uniform, we also continue to find some disc emission in the asymmetric maps. While this is possibly a sign of real structure, the minor levels of the remaining artifacts gives such a theory little weight.

The trajectories provide us with a way to estimate both disc dimensions and spot position; each marker represents a step of $0.1R_{L1}$ from the primary. For H α the ballistic trajectory gives a position for the brightest spot region at $R = (0.75 \pm 0.05)R_{L1}$; however, if the spot follows the Keplerian motion of the disc, the trajectory gives $R = (0.55 \pm 0.05)R_{L1}$. The inner edge of the hot spot should correspond to the outer disc edge and appears to extend as far up the Keplerian trajectory as $\sim 0.8R_{L1}$, close to the predicted outer disc truncation radius ($\sim 0.9R_{Roche} \sim 0.75R_{L1}$).

Figure 6 shows the tomograms and trails for H β . The weaker double peak translates into minimal disc structure in the maps, but as for H α what is visible of the disc remains relatively circular and uniform. The H β hot-spot position agrees very closely with that of H α , though appearing more circular. Figure 7 shows the relevant images for He I; being even weaker than H β , we can only make out the *s*-wave in the data without any detectable double-peak structure and subsequently only the hotspot appears in the maps, once again in the same position as the H lines. Since maximum-entropy regularisation cannot deal with negative

data points, in order to accommodate the Na I absorption line adjacent to He I we set the negative values to zero. This does not significantly affect the He I image since the absorption does not overlap the emission at any point.

In the case of Figure 8 (Ca II) we must make identical alterations to allow for the Ca II absorption within the emission pattern. While in this line there is some overlap between the Ca II emission and absorption, it only augments the maps since the absorption arises from the same transition as the emission, allowing DOPPLER to accurately reproduce the velocity location of the absorption. The maps show both the disc and hot spot, as well as the absorption region centered on the secondary's Roche lobe, confirming the mass donor as the source of these absorption lines. The disc in both the complete and asymmetric maps shows weak variation in intensity at locations similar to those seen in H α .

Finally, we have included tomograms of the four Na I absorption lines (Fig. 9). Spectra used for the images were created by zeroing neighboring emission or absorption lines to leave a single absorption *s*-wave (e.g., He I and Na I λ 5890 are reduced to leave λ 5896), and then the ordinate axis was inverted to create a negative with which DOPPLER can work. The maps clearly show the absorption centered on the centre of mass of the secondary. Hence, the Na I absorption seen in our spectra is a result of the secondary, and shifts with time due to its orbital motion.

Doppler tomograms: Figures 5–8 are mosaics of six images. The left-hand column (from top to bottom) shows the trailed spectra used to construct the maps, the Doppler map, and the reconstructed data from the map model. The right-hand column shows the trail from which a simulated axisymmetric component has been removed, the resulting asymmetrical component map, and the reconstructed data. The simulated symmetric image is created by finding median values for annular portions of the original map, centered on the velocity of the primary ($0, -K_1 \text{ km s}^{-1}$), and the predicted data/trail for this map is calculated and subtracted from the original data to give the asymmetric component. Overplotted onto the maps are the companion Roche lobe, predicted companion, primary and center-of-mass positions (crosses), and two lines representing the accretion stream ballistic trajectory (lower line) and the Keplerian velocity of the disc along the stream (upper line). The crosses along the trajectories represent steps of $0.1R_{L1}$ from the primary and asterisks show the apsides of the stream.

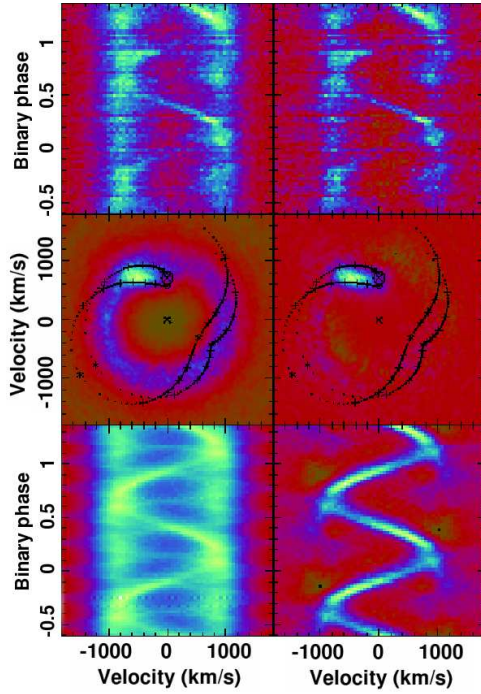


Figure 5. $H\alpha$ Doppler tomograms. The hot spot can be seen between the two trajectories in both middle panels. The circular disc is also clearly visible.

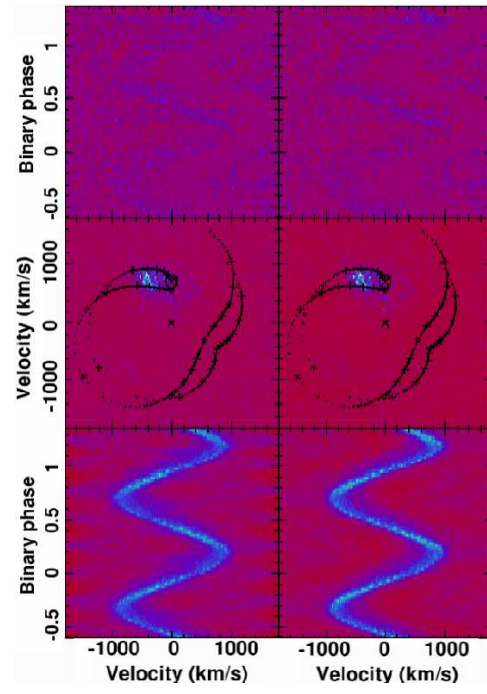


Figure 7. $He\ I$ Doppler tomograms. Only the hot spot is apparent.

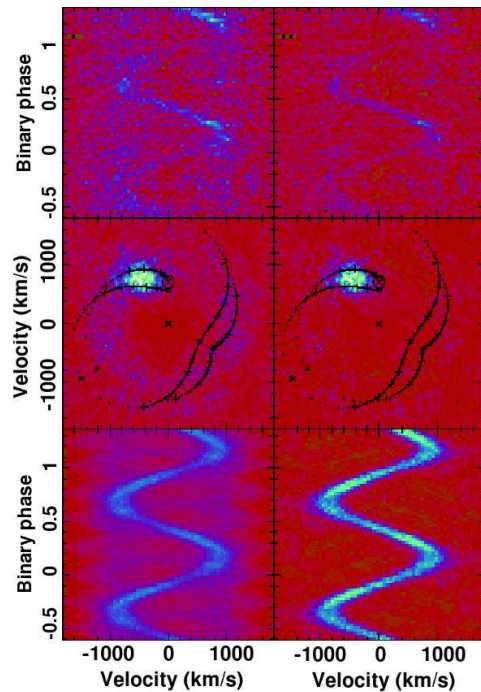


Figure 6. $H\beta$ Doppler tomograms. Again we observe the hot spot between the two trajectories, but the disc is barely detected.

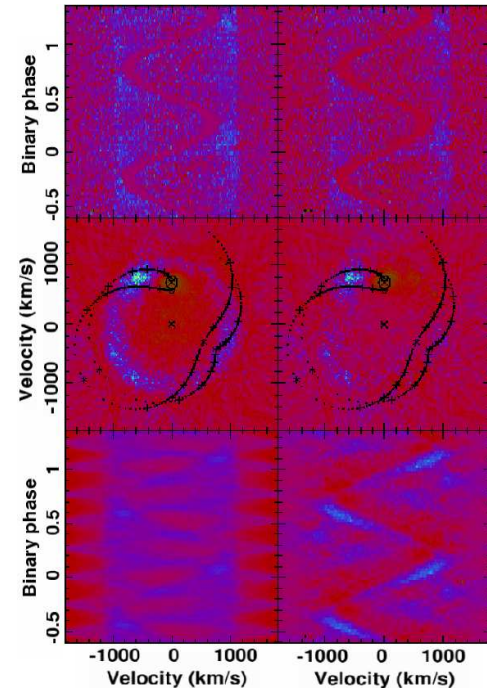


Figure 8. $Ca\ II\ \lambda 8662$ tomograms. The disc and hot spot remain clear and now we can also see absorption located at the secondary.

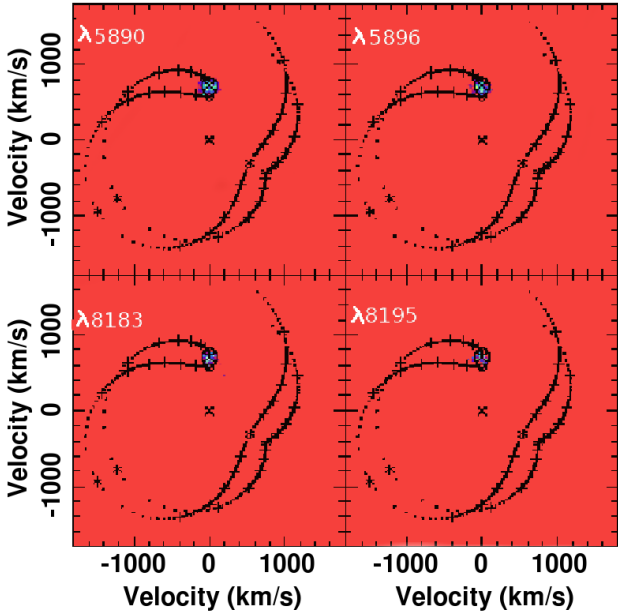


Figure 9. Na I λ 5890, λ 5896, λ 8183, and λ 8195 absorption Doppler tomograms. The absorption is clearly centered on the secondary’s position in all the images. Overplotted features match those described for earlier tomograms (see the top of the previous page).

4.2 Modulation tomography

As we have seen, the intrinsic variations associated with the emission of XTE J1118+480 can cause problems when producing Doppler tomograms. Though the maps are clearly useful in identifying structure within the disc, much of the behaviour we observe in the trails cannot be represented accurately. Modulation tomography overcomes the need to assume that the flux in the line remains constant over the orbit and allows us to map fluctuations as a function of orbital period. Though this makes the method more robust than Doppler tomography, it does require data having higher signal-to-noise ratio; hence, we apply this technique to the H α line alone. The process is described in detail by Steeghs (2003).

We note that for tomography one needs an accurate measurement of the systemic velocity of the binary system. In our case the systemic velocity is well constrained (2.7 ± 1 km s $^{-1}$) using the many absorption lines in the Keck data from the mass donor star (GH08). In addition, we tested the value of γ determined by GH08 by fitting the mean velocity for the sodium D absorption features and find 2.1 ± 2 km s $^{-1}$. The phase-invariant offset found in H α line emission (discussed earlier) needs to be taken into account when discussing disc structure since the visible disc’s centre may be offset compared to the primary via eccentricity. Modulation tomography results in four tomograms rather than one: an average map (akin to the original Doppler tomograms), a map detailing total modulated emission and finally maps that show the individual sine and cosine components of the modulated emission. The sine and cosine labels correspond to how the emission varies in relation to the phase; “sine” modulated variations are those that form a sine profile when plotted against phase (i.e., emission that peaks at phase 0.25

and has a minimum at phase 0.75), while “cosine” modulated variation would correspond to variations occurring in phase with a cosine profile (i.e., maxima/minima occurring at phases of 0, 0.5, and 1). Variation with a mixture of components are therefore those that appear in both maps.

We show modulation tomograms using the systemic velocity in Figure 10 and the offset velocity (in addition to systemic) in Figure 11. In Figure 10, the average or “constant” map closely resembles the original Doppler maps except the disc and hot spot are better defined, and there appears to be a component of emission lying over the Roche lobe of the secondary that was previously undetectable. The hot spot remains elongated and in a similar position to that in the Doppler maps, with an inner edge closer to $(0.75 \pm 0.05)R_{L1}$ ($\sim 0.9 R_{\text{Roche}}$); the estimated truncation radius (see Section 3.2). The color scale of the modulation maps represents a much smaller dynamic range than that of the Doppler maps; the observed effects are weak and do not necessarily dominate the behaviour of the overall system.

The hot spot appears in both cosine and sine component maps. Green and red components of the spot in the cosine map represent regions which brighten at opposite phases to each other, caused by exposure of different faces of the extended stream-disc interaction as phase varies. Both the green and red regions reside near $0.8R_{L1}$ along the ballistic trajectory. The hot spot in the sine map is dominated by a single green/white region that resides just above the ballistic trajectory at $0.7R_{L1}$. The disc also appears to show modulated variation in both component maps. The cosine map shows strong variation in the slower (inner map) disc regions that vary opposite in phase. A similar but weaker crescent appears in the lower half of the sine map. The crescent regions appear to be modulated at the orbital period, as suggested by their positions and relative amplitudes in both maps, rotated by 90 degrees in relation to each other. At first this might imply a stationary (from an observer’s point of view) bright region which moves within the disc as the system rotates, but we have yet to include the effects of the 54.6 km s $^{-1}$ offset. The overall variation in the disc is easier to discern in the final amplitude map (centre-right panel of Fig. 10). We can see some disc variation at higher velocities in the lower-left quadrant, but most is confined to the hot spot and slower disc regions. However, due to the nature of the H α shift, these disc structures are not real but once again a byproduct of not taking the velocity offset into account.

Finally, notice that the modulated model data resemble the original data far more closely than the unmodulated Doppler maps of Figure 5, including the correct variation in *s*-wave and red-peak intensities. The gap seen in the data is real and corresponds to the larger than average gap in phase between observations 30 and 31 (see Table 2). It is visible here (unlike in the Doppler tomography mosaics) due to the higher resolution of the modulation tomography plotting routines.

Figure 11 shows the modulation map which uses the measured centroid offset of the H α line as the systemic velocity. The accretion disc appears remarkably symmetric, with little azimuthal structure in the constant map and no significant modulation in the amplitude map. The bright spot stands out nicely, and as can be seen from the plot, varies in strength by about 25%. The predominant positive

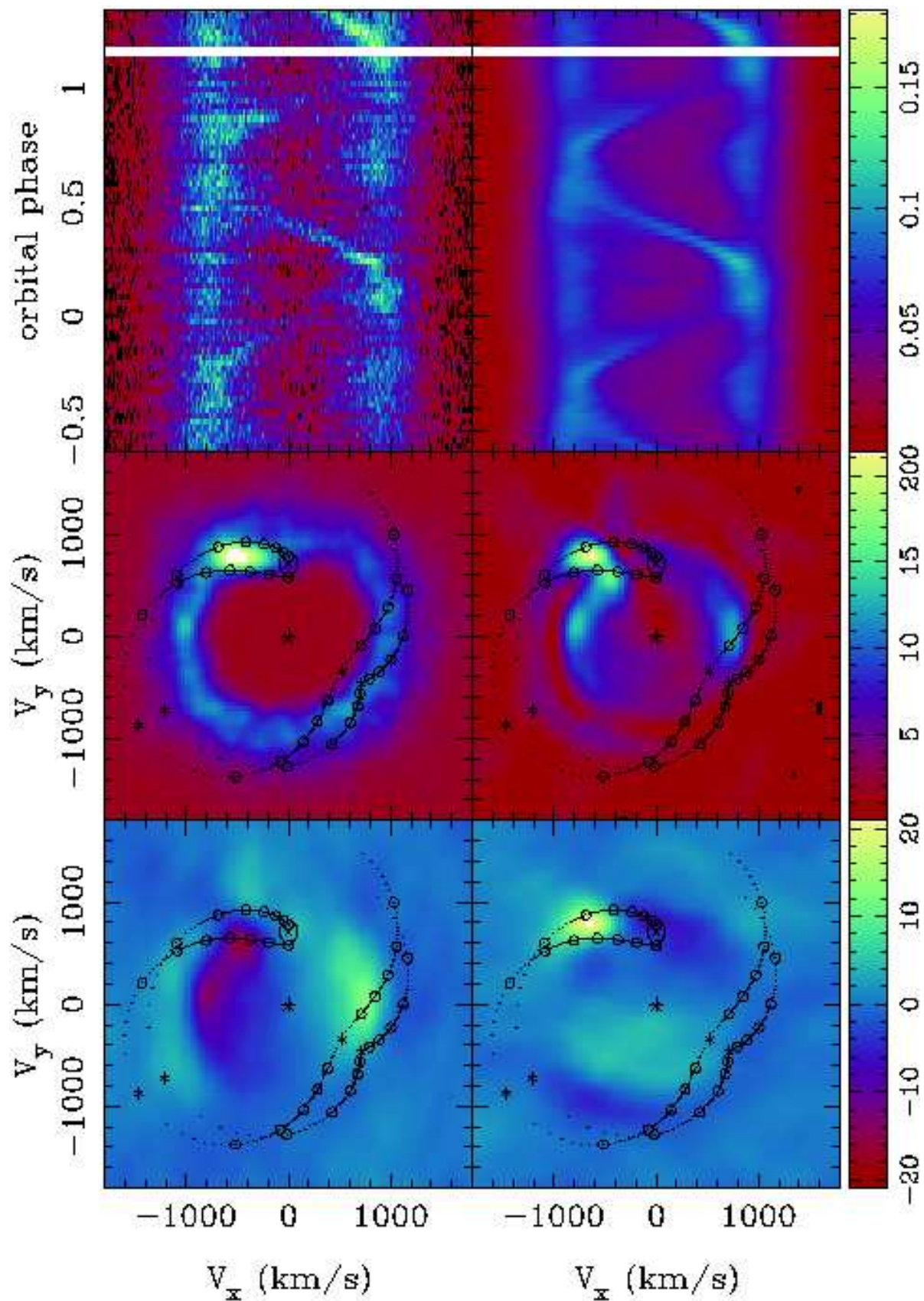


Figure 10. $H\alpha$ modulation tomograms using $\gamma = 2.7 \text{ km s}^{-1}$. The observed data (top left) are well reproduced by the fitted data (top right). The middle left-hand panel shows the constant part of the disc with a strong hot spot, and the middle right-hand panel illustrates the amplitude of the modulation. The bottom row represents the cosine (left) and sine (right) components of rotation.

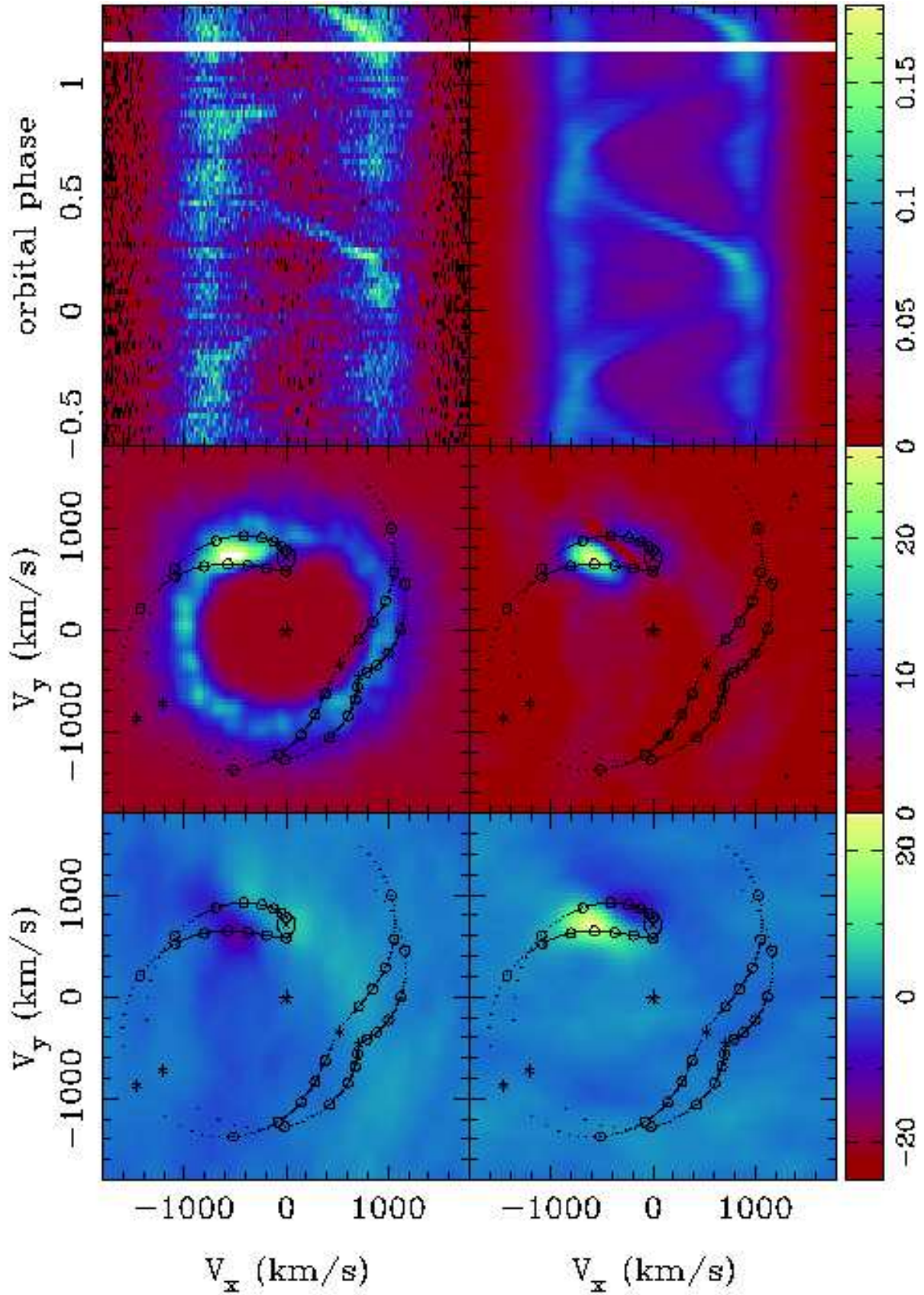


Figure 11. $H\alpha$ modulation tomograms taking the measured centroid of the $H\alpha$ line as the systemic velocity ($\gamma = +57.3 \text{ km s}^{-1}$). The stream for $q = 0.024$ is also plotted, using $\gamma = 57.3 \text{ km s}^{-1}$. The observed data (top left) are well reproduced by the fitted data (top right). The middle left-hand panel shows the constant part of the disc with a strong hot spot, and the middle right-hand panel illustrates the amplitude of the modulation. The bottom row represents the cosine (left) and sine (right) components of radiation.

sine term reflects the fact that the hot spot is brightest near phase 0.25 (i.e., like the maximum of a sine wave). The location of the hot spot itself is stable, peaking at $R = 0.7R_{L1}$ on the ballistic trajectory and with some mixing of disc velocities. Though the spot appears at different positions in the sine and cosine maps, this is not a physical movement; the sine and cosine maps show how the anisotropic emission from the stream-impact point causes the emission to modulate over phase. Near phase 0.25 one looks more directly into the impact site resulting in the peak in emission. This disc appears relatively stable and quiet (lacking any signs of eccentricity). Only a long observing run covering the precession cycle could confirm if the disc is able to remain circular and isotropic in its emission, yet still precess.

5 DISCUSSION AND CONCLUSIONS

5.1 XTE J1118+480 accretion in quiescence

Tomograms constructed using $H\alpha$ as well as emission from $H\beta$, He I $\lambda 5876$, and Ca II $\lambda 8662$ each reveal a well-defined hot spot lying, as expected, between the ballistic stream and Keplerian disc velocity, where the accretion stream hits the disc. To04 saw no evidence for a hot spot in $H\alpha$ during observations taken in 2003 January; instead, they report that the asymmetric component of the map showed emission centered on the secondary's Roche lobe, suggesting that mass transfer had dropped significantly or ceased during the system's quiescent period. We propose that during our observation mass-transfer has resumed (producing a hot spot) although there is still minimal accretion onto the compact object, keeping the system in quiescence.

The peak-to-peak separation of the $H\alpha$ profile during our observations is quite large and appears to be a sign of relative quiescence. During the rather large outburst in Mar–Apr 2000 the peak-to-peak separation was at its lowest; during the “mini-outburst” of 2005 the peak-to-peak separation is somewhat larger but still significantly smaller than during true quiescence.

5.2 Imaging of the donor star and resolution of column density

Because of its high Galactic latitude, the interstellar absorption toward XTE J1118+480 is very low. Garcia et al. (2000) limited $E(B - V)$ to 0.024 mag. Using multiwavelength observations spanning the energy range 0.4–160 keV, McClintock et al. (2001b) constrained the column density to $N_H = 1.2 \times 10^{20} \text{ cm}^{-2}$, consistent with the Garcia et al. optical measurement. Although Dubus et al. (2001) claimed $N_H = 1.8 \times 10^{20} \text{ cm}^{-2}$, Chaty et al. (2003) showed that such high column densities are inconsistent with accretion-disc models. Dubus et al. (2001) measured their column densities by using fits to Ca II absorption features that they attributed to interstellar absorption based on their spectral similarity to the Na I D lines. Our tomograms show unequivocally that the strong absorption features of Ca II and Na I are due entirely to the late-type secondary. Doppler maps of the absorption lines of Na I $\lambda\lambda$ 5890, 5896, 8183, 8195 and Ca II $\lambda 8662$ clearly demonstrate their origin from the donor star. Trained spectra of many weaker absorption features (some of

which are visible in Fig. 4) show the same s -wave pattern, indicating that they also originate from the donor star. We suggest that the high N_H measured by Dubus et al. (2001) is incorrect because of their erroneous interpretation of Ca II absorption features as being of interstellar origin.

5.3 Evidence for continuing precession and disc eccentricity

Our Doppler tomograms show a disc that is relatively circular and uniform in comparison to those presented by To02 and To04. For the modulation maps which are more sensitive to effects that change over the orbital period, asymmetric effects are only apparent when we use the systemic velocity of the system. The modulation effects disappear when we use our measured velocity offset of 55 km s^{-1} and instead we see a circular disc with isotropic emission.

Zu02 found a superhump period 0.3% larger than the orbital period in XTE J1118+480, implying a precession period of about 52 days. Their analysis of offsets in the centroid of $H\alpha$ emission were consistent with a 52 day precession period. $H\alpha$ offsets measured by To04 up to two years after Zu02 showed that the precession period persisted. Gelino et al. (2006) and Shahbaz et al. (2005) did not detect superhump periods, but their observations were not sensitive to effects below the 0.5% level. Our measurement of an offset in the $H\alpha$ centroid is consistent with effects from a precessing eccentric disc with a precession period of 51.42 ± 0.05 days. However the fit requires the assumption that the precession period remains stable over long periods of time and hence in various system states, which is unprovable using existing offset measurements.

Zu02 compared XTE J1118+480 to SU UMa systems because of the superhump effect they detected, but we note that in SU UMa systems superhump effects are seen only in outburst. In the case of XTE J1118+480, the mass ratio ($q = 0.024$) is extreme enough to allow for effects of the 2:1 tidal resonance that is not possible with SU UMa dwarf novae (Whitehurst & King 1991). Indeed, we find that the outer radius of our disc extends well beyond the 3:1 and 2:1 tidal resonance radii, supporting the continued presence of precession.

However, we are now left with the paradox of observing a circular, uniform accretion disc that shows evidence of effects associated with eccentricity, namely the emission-line offset. A physical scenario for this would be a circular disc in which the matter's orbital velocity varies with phase. The cause could be a slight offset in the disc centre's position (i.e., not the same as the position of the primary's centre of mass). This is obviously an unstable situation, and in turn unlikely to be observed; however, we must consider two other factors before discarding it as a solution. Firstly, compared to values previously measured for the offset (e.g., 250 km s^{-1} in Zu02) our offset is small, which could in turn suggest a lower degree of eccentricity required to cause it (i.e., too slight to detect). This is difficult to confirm without additional observations covering more of the precession cycle. Secondly, it is possible we are simply not observing enough of the disc at our chosen wavelengths to detect the full extent of the eccentricity. Referring to the dissipation maps in Figure 4 of Foulkes et al. (2004), were we ignorant of the inner half of the disc, the remaining portion (especially the outer

edge) would appear very circular and yet have the required offset to fulfill the above scenario. We may have essentially caught the system during a short-lived arrangement.

6 SUMMARY

We have presented emission-line analysis, Doppler tomography, and modulation tomography of XRN XTE J1118+480 from Keck spectra taken on the night of 2004 Feb. 14 when the system was in X-ray quiescence. All emission tomograms reveal a well-defined hot spot lying between ballistic stream and Keplerian disc velocity trajectories, and the strongest emission lines clearly show the disc. The hot spot implies that mass transfer is ongoing, although accretion onto the compact object is at a minimal level. Applying the orbital solution from GH08, tomography of several absorption lines allows us to reveal the companion star. The peak-to-peak velocity of the H α profile is significantly larger during quiescence, as expected since the disc is smaller. Measurement of the H α offsets suggest the presence of a precessing accretion disc. Using our measured H α centroid offset of 55 km s⁻¹ instead of the systemic velocity in modulation mapping, anisotropic features are eliminated, producing a relatively circular, isotropic disc. Precession can be sustained because the disc extends beyond the 3:1 and 2:1 tidal resonance radii, but we need more observations at different precession phases in order to determine how the offset we measure is affected by precession effects and how they compare to those observed in the past.

7 ACKNOWLEDGEMENTS

The W. M. Keck Observatory is operated as a scientific partnership among the California Institute of Technology, the University of California, and NASA; it was made possible by the generous financial support of the W. M. Keck Foundation. We thank the Keck staff, as well as Ryan Chornock, for their assistance with the observations. The ASM data are provided by the ASM/RXTE teams at MIT and at the RXTE SOF and GOF at NASA's GSFC. We acknowledge use of the MOLLY, DOPPLER, and TRAILER software developed by Tom Marsh, MODMAP developed by Danny Steeghs, and the NIST Atomic Spectra Database. This work was supported by NSF grants AST-0507637 to SDV and AST-0607485 to AVF. JIGH acknowledges support from European Commission contract MEXT-CT-2004-014265 (CIFIST).

REFERENCES

- Chaty, S., Haswell, C. A., Malzac, J., Hynes, R. I., Shrader, C. R., & Cui, W., 2003, *MNRAS*, 346, 689
- Chen, W., Shrader, C. R., & Livio, M., 1997, *ApJ*, 491, 312
- Dubus, G., Kim, R. S. J., Menou, K., Szkody, P., & Bowen, D. V., 2001, *ApJ*, 553, 307
- Elebert, P., Callanan, P.J., & Torres, M.A.P., 2006, in *Populations of High Energy Sources in Galaxies*, Proceedings of IAU Symposium No. 230. E. J. A. Meurs & G. Fabbiano, eds. (Cambridge: Cambridge University Press), 57
- Foulkes, S. B., Haswell, C. A., Murray, J. R., & Rolfe, D. J., 2004, *MNRAS*, 349, 1179
- Garcia, M., Brown, W., Pahre, M., McClintock, J., Callanan, P., & Garnavich, P., 2000, *IAU Circ.* 7392
- Gelino, D. M., Balman, Ş., Kızıloğlu, Ü., Yılmaz, A., Kalemci, E., & Tomsick, J. A., 2006, *ApJ*, 642, 438
- González Hernández, J. I., Rebolo, R., Israelian, G., Filippenko, A. V., Chornock, R., Tominaga, N., Umeda, H., & Nomoto, K. 2008, *Apj*, 679, 732 (GH08)
- González Hernández, J. I., Rebolo, R., Israelian, G., Harlaftis, E. T., Filippenko, A. V., & Chornock, R., 2006, *ApJ*, 644, L49 (GH06)
- Jahoda, K., Swank, J. H., Giles, A. B., Stark, M. J., Strohmayer, T., Zhang, W., Morgan, E. H., 1996, *SPIE*, 2808, 59
- King, A., 1995, in *X-ray binaries*, Cambridge Astrophysics Series 26, W. H. G. Lewin, J. van Paradijs, & E. P. J. van den Heuvel, eds. (Cambridge: Cambridge University Press), 419
- Levine, A. M. et al., 1994, *ApJ*, 469 33
- Marsh, T. R., 2001, in *Lecture Notes in Physics: Astrotomography, Indirect Imaging Methods in Observational Astronomy* (Berlin: Springer Verlag), 573
- Marsh, T. R., & Horne, K., 1988, *MNRAS*, 235, 269
- Marsh, T. R., Robinson, E. L., & Wood, J. H., 1994, *MNRAS*, 266, 137
- McClintock, J. E., Garcia, M. R., Caldwell, N., Falco, E. E., Garnavich, P. M., & Zhao, P., 2001a, *ApJ*, 551, L147
- McClintock, J. E., et al., 2001b, *ApJ*, 555, 477
- Meyer, F., & Meyer-Hofmeister, E., 1981, *A&A*, 104, L10
- Neilsen, J., Steeghs, D., & Vrtilik, S. D., 2008, *MNRAS*, 384, 849
- Patterson, J., et al., 2000, *IAU Circ.* 7412
- Remillard, R., Morgan, E., Smith, D., & Smith, E., 2000, *IAU Circ.* 7389
- Shahbaz, T., et al., 2005, *MNRAS*, 362, 975
- Sheinis, A. I., Bolte, M., Epps, H. W., Kibrick, R. I., Miller, J. S., Radovan, M. V., Bigelow, B. C., & Sutin, B. M., 2002, *PASP*, 114, 851
- Steeeghs, D., 2003, *MNRAS*, 344, 448
- Torres, M. A. P., et al., 2002, *ApJ*, 569, 423 [To02]
- Torres, M. A. P., Callanan, P. J., Garcia, M. R., Zhao, P., Laycock, S., & Kong, A. K. H., 2004, *ApJ*, 612, 1026 [To04]
- Uemura, M., Kato, T., Yamaoka, H., Buczynski, D., Takamizawa, K., & Trondal, O., 2000a, *IAU Circ.* 7390
- Uemura, M., et al., 2000b, *PASJ*, 52, L15
- Uemura, M., et al., 2000c, *IAU Circ.* 7418
- Wagner, R. M., Foltz, C. B., Shahbaz, T., Casares, J., Charles, P. A., Starrfield, S. G., & Hewett, P., 2001, *ApJ*, 556, 42
- Whitehurst, R., & King, A., 1991, *MNRAS*, 249, 25
- Zurita, C., et al., 2002, *MNRAS*, 333, 791 [Zu02]
- Zurita, C., et al., 2006, *ApJ*, 644, 432